



1 Salt intrusion dynamics in a well-mixed sub-estuary connected to a
2 partially to well-mixed main estuary

3 Zhongyuan Lin^{c,d}, Guang Zhang^{a,b}, Huazhi Zou^{c,d}, Wenping Gong^{a,b*}

4 ^aSchool of Marine Sciences, Sun Yat-sen University, Zhuhai, 519082, China

5 ^bGuangdong Provincial Key Laboratory of Marine Resources and Coastal Engineering, Zhuhai,
6 519082, China

7 ^c Key Laboratory of Pearl River Estuary Regulation and Protection of Ministry of Water
8 Resource, Guangzhou 510611, China

9 ^d Pearl River Water Resource Research Institute, Guangzhou 510611, China

10

11 Corresponding Author: Wenping Gong (gongwp@mail.sysu.edu.cn)

12

13

14 **Abstract**

15

16 Salt intrusion in estuaries has been exacerbated by climate change and human
17 activities. Previous studies have primarily focused on salt intrusion in the mainstem of
18 estuaries, whereas those in sub-estuaries (those branch off their main estuaries) have
19 received less attention. During an extended La Niña event from 2021 to 2022, a sub-
20 estuary (the East River estuary) alongside the Pearl River Estuary, China, experienced
21 severe salt intrusion, posing a threat to the freshwater supply in the surrounding area.

22 Observations revealed that maximum salinities in the main estuary typically preceded
23 spring tides, exhibiting significant asymmetry in salinity rise and fall over a fortnightly
24 timescale. In contrast, in the upstream region of the sub-estuary, the variation of salinity
25 was in phase with that of the tidal range, and salinity rise and fall exhibited more
26 symmetrical.

27 Inspired by these observations, we employed idealized numerical models and
28 analytical solutions to investigate the underlying physics behind these behaviors. It was



29 discovered that under normal dry condition (with a river discharge of $1500 \text{ m}^3 \text{ s}^{-1}$ at the
30 head of the main estuary), the river-tide interaction and change in horizontal dispersion
31 accounted for the in-phase relationship between the salinity and tidal range in the
32 upstream region of the sub-estuary. Under extremely dry conditions (i.e., a river
33 discharge of $500 \text{ m}^3 \text{ s}^{-1}$ at the head of the main estuary), salinity variations were in-
34 phase with those of the tidal range in the middle as well as the upstream region of the
35 sub-estuary. The variation of salinity in the main estuary, along with those of salt
36 dispersion and freshwater influx inside the sub-estuary collectively influenced salinity
37 variation in the well-mixed sub-estuary. These findings have important implications for
38 water resource management and salt intrusion prevention in the catchment area.

39 **Keywords:** Sub-estuaries; River-tide interaction; Partially to well-mixed estuary.

40

41 **1. Introduction**

42

43 Salt intrusion in estuaries has emerged as an increasingly significant
44 environmental issue, as it contaminates water quality, restricts freshwater supply, and
45 affects the biota's habitat in estuaries (Payo-Payo et al., 2022). The severity of salt
46 intrusion in estuaries has been further exacerbated by both climate change and
47 anthropogenic activities. Climate change has led to more severe droughts in various
48 regions worldwide (Spinoni et al., 2014), resulting in reduced freshwater flow from
49 upstream watershed basin into estuaries. In turn, this has intensified salt intrusion in
50 these areas. Additionally, sea level rise has been identified as a contributing factor to



51 this phenomenon (e.g., Hong et al., 2020). Human activities, including dam
52 construction in the watershed, channel dredging, and land reclamation in estuaries, have
53 caused reductions in river inflow, channel deepening, and enhanced convergence of
54 estuarine geometry, all of which favor an increase in salt intrusion (e.g., Ralston and
55 Geyer, 2019).

56 Salt intrusion in estuaries is the result of landward salt transport, which consists of
57 steady shear and tidal oscillatory transport (MacCready and Geyer, 2010). The
58 combination of estuarine circulation and salinity stratification induces a steady shear
59 when averaged in a tidal cycle. Tidal oscillatory transport is generated by tidal pumping
60 such as the jet-sink flow for an inlet (Stommel and Farmer, 1952), tidal trapping with a
61 side embayment (Okubo, 1973), tidal shear dispersion by the vertical shears of current
62 and mixing (Bowden, 1965), tidal straining (Simpson et al., 1990), and chaotic stirring
63 (Zimmerman, 1986).

64 In general, for a partially mixed estuary in which the steady shear dominates the
65 landward salt transport, the salt intrusion is strongest during neap tides and weakest
66 during spring tides under the steady-state conditions, meaning that the change in salinity
67 is out-of-phase with that in the tidal range. However, for a well-mixed and/or a salt
68 wedge estuary, in which the tidal dispersion is the dominant contributor to landward
69 salt transport, the salt intrusion is strongest during spring tides and weakest during neap
70 tides, signifying that the salinity variation is in phase with the tidal range (Ralston et
71 al., 2010). These steady-state situations are altered by the unsteadiness of external
72 forcing and the adjustment of estuaries to the changing forcings (Chen 2015 and



73 references therein). In general, when the internal timescale of an estuary, which is
74 defined as the time needed for a water parcel from the upstream to travel through the
75 estuary by the river-induced flow, is shorter than the external timescale, which is often
76 the spring-neap tidal cycle, the salinity variation in an estuary can keep pace with the
77 change in tidal forcing and reaches steady state. However, when the internal timescale
78 is longer than the external timescale, the salt intrusion can hardly reach the steady state,
79 and there exists a phase shift between the salt intrusion and tidal range, such as in the
80 Modaomen estuary (Gong and Shen, 2011) and Hudson River (Bowen and Geyer,
81 2003).

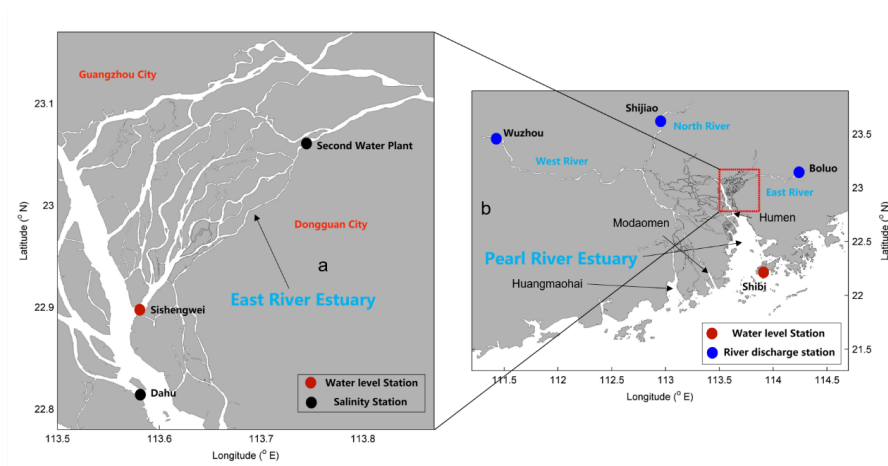
82 Previous studies on salt intrusion have primarily focused on main estuaries, where
83 freshwater discharge empties into the estuarine waterbody at the estuary head and is
84 profoundly diluted by the seawater from the ocean. However, there has been relatively
85 less research on salinity dynamics specifically in tidal creeks or sub-estuaries, i.e. those
86 that reside aside from their main estuary. It is worth noting that larger estuaries often
87 possess sub-estuaries or tidal creeks, as highlighted by Uncles and Stephens (2010).
88 Sub-estuaries branch off the stem of their main estuary and exhibit behavior that is
89 partially dependent on processes acting within the main estuary. Haywood et al. (1982)
90 described the importance of conditions at the confluence of the York River sub-estuary
91 and the Chesapeake Bay to salinity stratification within the sub-estuary. Uncles and
92 Stephens (2010) investigated the salinity dynamics in a sub-estuary (Tavy) connected
93 to the main estuary (Tamar, UK). They noted that the tidal range had a limited effect on
94 the salinity in the sub-estuary. Yellen et al. (2017) examined the sediment dynamics in



95 a side embayment of the main estuary of Connecticut, USA, and found that salinity
96 intrusion from the main estuary enhanced sediment trapping inside the sub-estuary.

97 The previous studies on sub-estuary salt dynamics have mainly focused on
98 examining salinity variabilities and water column stratification, as exemplified by the
99 work of Haywood et al. (1982). Some investigations have also explored the influence
100 of river discharge from the heads of the main estuary and sub-estuary, as well as the
101 impact of winds, as discussed by Uncles and Stephens (2010). However, there remains
102 a knowledge gap regarding how the salt dynamics in the main estuary affect those in
103 the sub-estuary, as well as how the interaction between river flow and tides influences
104 salinity variations in the sub-estuary. Regarding the river-tide interaction, here we focus
105 on how tides affect river flow through mechanisms such as nonlinear bottom friction
106 and advective terms in the momentum equation, as outlined by Buschman et al. (2009),
107 whereas the effect of river flow on tidal propagation will not be explored.

108 In 2021, under the influence of a La Nina event, the precipitation in the Pearl River
109 Delta (PRD) area (Fig. 1), China, was extremely low, and the salt intrusion was very
110 severe, which imposed a great threat to the freshwater supply in the region, especially
111 during winter months (December to February). Alongside the Pearl River Estuary
112 (PRE), a sub-estuary of the East River estuary (Fig. 1), also experienced strong salt
113 intrusion and heavily impacted the water supply to the city of Dongguan, home to a
114 population of 10 million people. This shortage of freshwater became a significant
115 concern for the surrounding people, especially during the Spring Festival, the Chinese
116 Lunar New Year.



117

118 Fig.1. a) The East River estuary; b) Map of the Pearl River Delta and the locations of hydrological

119 and water level stations.

120

121 The present work has two objectives: (a) to investigate the characteristics of salt
122 intrusion in a well-mixed sub-estuary by analyzing observation data. The characteristics
123 include spatial-temporal variations of salt intrusion and its relationship with river flow
124 and tidal range; (b) to explore the underlying physics behind salt intrusion in the sub-
125 estuary, such as the impacts of salt dynamics in the main estuary, and the river-tide
126 interaction inside the sub-estuary. To achieve the above goals, we first collected and
127 analyzed observational data of salt intrusion at the East River estuary. Then we utilized
128 an idealized configuration for numerical model investigation. Two numerical model
129 experiments with mean and extremely low river discharges in dry seasons in the main
130 estuary, respectively, were conducted to identify the relevant mechanisms for the
131 variability of salt intrusion in the sub-estuary. Furthermore, to clearly understand the
132 phase relationship between salinity and tidal range, analytical solutions for the subtidal



133 salinity in the well-mixed sub-estuary were utilized.

134 The remainder of this paper is structured as follows. The study site is briefly
135 introduced in Section 2. The methods of data analysis, numerical model simulation, and
136 analytical solution are presented in Section 3. In Section 4, the results of the salt
137 intrusion dynamics through the measurement data analysis, numerical model, and
138 analytical solution are demonstrated, followed by some discussions on the impacts of
139 river-tide interaction in the sub-estuary, the salt dynamics in the main estuary, and the
140 limitations of this study in Section 5. Finally, a summary and conclusion are given in
141 Section 6.

142

143 **2. Study site**

144

145 The Pearl River, China's second largest river in terms of annual freshwater
146 discharge, has three main branches: West River, North River, and East River (Hu et al.,
147 2011), as displayed in Fig. 1b. The Pearl River forms a complex delta, known as the
148 Pearl River Delta (PRD), which consists of the downstream river network and three
149 estuaries, from west to east: the Huangmaohai Estuary, the Modaomen Estuary, and the
150 PRE (Fig. 1b). The PRE, the largest of the three estuaries, is funnel-shaped and has a
151 mean depth of 4.6 m (Wu et al., 2016). Its width decreases from 50 km at its mouth
152 between Hong Kong and Macau to 6 km at Humen Outlet. The axial length of the
153 estuary from the mouth to Humen is approximately 70 km. Above the Humen, the
154 estuary becomes relatively straight and further extends almost 90 km landward to its
155 head. Upstream of the Humen, there exists a waterway known as Shizhiyang. Along the



156 waterway, there are several river tributaries, among which the East River sub-estuary,
157 are distributed on the east side.

158 The river discharge into the PRE is about 1/4 of the total river flow from the Pearl
159 River. The total annual river discharge of the Pearl River is $3260 \times 10^8 \text{ m}^3$, in which the
160 river discharge experiences distinct seasonal variations. During the dry season (from
161 November to March), the river discharge at the head of the Pearl River takes up only
162 about 30% of the annual discharge, so the total river discharge of the Pearl River is
163 about $6000 \text{ m}^3/\text{s}$ in the dry season, and the upstream river discharge of the PRE is 1500
164 m^3/s (1/4 of the total). Under extremely dry conditions, the river discharge at the head
165 of the PRE can be less than $1000 \text{ m}^3/\text{s}$.

166 The PRE has a microtidal and mixed semi-diurnal regime (Mao et al., 2004). The
167 annual mean tidal range is 1.45 m near Lantau Island (at the mouth of the PRE) and
168 1.77 m near the Humen outlet (Gong et al., 2018). The amplitudes of M_2 , S_2 , K_1 , and O_1
169 constituents near the Lantau Island are 35.5, 14, 33.5, and 27.9 cm, respectively (Mao
170 et al., 2004), showing the dominance of the M_2 constituent. The alternation of neap and
171 spring tides causes the tidal range near Lantau Island to vary from approximately 0.7 m
172 during neap tides to approximately 2 m during spring tides. Apart from the fortnightly
173 variation of the tidal range, there also exists a monthly variation, which is referred to as
174 the apogee/perigee cycle (Payo-Payo et al., 2022).

175 The PRE exhibits strong seasonal variation and is highly stratified during the wet
176 summer season (July to September), with the bottom isohaline of 10 psu protruding into
177 the upper estuary (50 to 70 km from the estuary mouth) and the surface isohaline of 10



178 psu extending outside of the estuary. The subtidal bottom-surface salinity difference is
179 mostly greater than 10 psu inside the estuary (Dong et al., 2004). During the dry season,
180 the PRE is generally in a partially mixed state, with the bottom isohaline of 10 psu
181 reaching the Humen Outlet, and the surface isohaline of 10 psu lying in the upper
182 estuary (Wong et al., 2003; Gong et al., 2018). In the dry season, the horizontal
183 difference of depth-mean salinity varies by between 20 and 25 psu across a distance of
184 70 km from the estuary mouth to Humen Outlet, and the vertical salinity difference
185 between the surface and bottom varies from 1 to 12 psu along the channels in the estuary.

186 The East River is a branch of the Pearl River, with a length of 562 km and a
187 drainage area of 27,040 km². It forms a sub-delta, known as the East River Delta, which
188 is located on the east side of the PRE and above the Humen Outlet (Fig. 1a). The upper
189 reach of the East River is essentially composed of a single channel, while in its lower
190 reach, downstream of Dongguan City, a complex river network is formed, including
191 several tributaries (Fig. 1a). Here we focus on the southernmost tributary, which merges
192 into the main estuary at the confluence of Sishengwei, where a hydrological station
193 resides. This tributary has a length of approximately 75 km from the confluence
194 (Sishengwei) to the upstream hydrological station of Boluo (Fig. 1b), and a mean water
195 depth of less than 5 m.

196 The average annual freshwater load of the East River is $240 \times 10^8 \text{ m}^3$, or a mean
197 river discharge of $728 \text{ m}^3 \text{ s}^{-1}$, accounting for 7.1% of the total river flow of the Pearl
198 River. During dry seasons, the river discharge is approximately $400 \text{ m}^3 \text{ s}^{-1}$. However,
199 the annual mean river discharge in 2021 was only $262 \text{ m}^3 \text{ s}^{-1}$. During the winter of 2021,



200 the salinity at several water plants exceeded the drinking water criteria of 0.5 psu for a
201 lasting duration of 3 months and impaired the freshwater supply in the region.

202 Similar to the main estuary, the tidal regime in the East River sub-estuary is a
203 mixed semi-diurnal one, with the tidal range decreasing when propagating upstream
204 due to the predominance of the bottom friction over the estuarine convergence. In recent
205 decades, the tidal strength has been seen to increase by human activities, such as sand
206 mining in the estuary (Jia et al., 2006).

207

208 **3. Methods**

209

210 **3.1 Observation data and analysis**

211

212 The observation data here consist of the daily discharge of the West, North, and
213 East Rivers, hourly water level data at the confluence (Sishengwei) between the East
214 River sub-estuary and the main estuary (PRE), daily sea level at the mouth of the PRE
215 (Shibi), and hourly surface salinity data at the Dahu station, which is located
216 downstream of the Sishengwei, and at the Second Water Plant of Dongguan City. These
217 two stations span a distance of approximately 30 km. The river discharge data at three
218 river branches of the Pearl River, hourly water level data at Sishengwei, and hourly
219 surface salinity data at Dahu are from the Pearl River Water Resources Commission,
220 whereas the salinity data at the Second Water Plant is from the Water Authority of
221 Dongguan City. The sea level data at the estuary mouth is from the Hong Kong
222 Observatory (<http://gb.weather.gov.hk/contentc.htm>). All the salinity data are the



223 surface salinities.

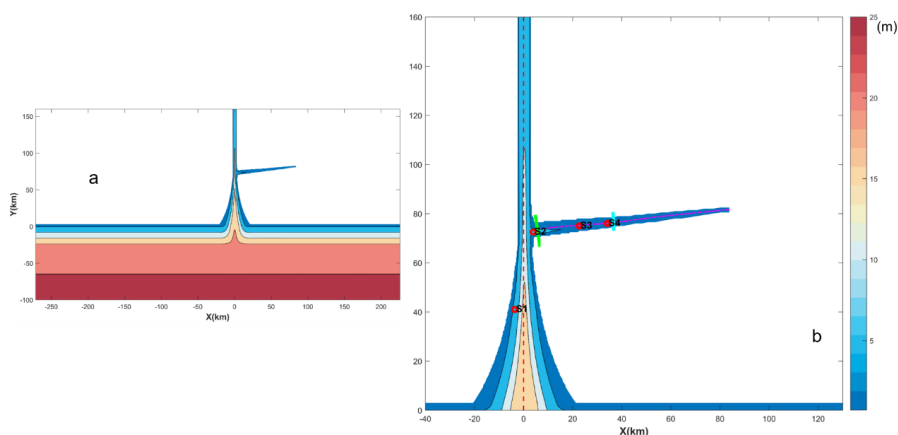
224 The salinity data at the Second Water Plant was subject to wavelet analysis, a
225 method that has been widely used to analyze geophysical data, like in salt intrusion
226 studies in estuaries (Liu et al., 2014; Gong et al., 2022). This method can identify
227 localized periodicities (or bands) that are linked to specific processes, such as tidal and
228 spring-neap variations. In this study, the continuous wavelet transform (CWT) method
229 was used to identify the multi-scale characteristics of salinity, and cross wavelet was
230 employed to examine the nonlinear correlations among variables, such as between the
231 salinity of the Second Water Plant and the water level at Sishengwei, between the
232 salinity of the Second Water Plant and the salinity of Dahu, and between the salinity of
233 the Second Water Plant and the river discharge at the Boluo Station.

234

235 **3.2 Numerical model configuration and experiments**

236

237 The Regional Ocean Modeling System (ROMS) was used in this modeling study.
238 ROMS is a free-surface, hydrostatic, primitive-equations ocean model that uses
239 stretched, terrain-following vertical coordinates and orthogonal curvilinear horizontal
240 coordinates on an Arakawa C-grid (Haidvogel et al. 2000). The model domain was
241 designed as an estuary-shelf system (Fig. 2). In the coordinate system, x is in the



242

243 Fig. 2. Geometry and bathymetry of the idealized model domain: a)for the whole domain;

244 b)zoom in for the area of concern. The origin of the coordinates is in the middle of the main

245 estuary mouth. The longitudinal sections in the main and sub-estuary are shown as dashed lines,

246 and the cross-sections inside the sub-estuary are shown as color solid lines. The locations of

247 several stations are indicated.

248

249 cross-estuary direction, with rightward being positive, y is in the along-channel

250 direction, with landward being positive, and z directs upward. The origin of the

251 system is in the middle of the estuary mouth. The estuary is composed of a convergent

252 part and a straight part. The geometry and bathymetry of the estuary roughly resemble

253 those of the PRE, with the convergent part extending from the estuary mouth to the

254 Humen Outlet (70 km in length), and the straight part from the Humen Outlet to the

255 head of the estuary (90 km long). For the convergent part, the estuarine width B is

256 assumed to decrease exponentially in the landward direction, as follows:

257
$$B = B_0 \exp\left(-\frac{y}{L_b}\right) \quad (1)$$

258 where B_0 is the estuarine width at the estuary mouth (here taken as 46 km) and L_b is



259 the width convergence length (taken as 31 km, as estimated by Zhang et al., 2021). The
260 bathymetry of the PRE is characterized by deep channels and side shallow shoals. We
261 roughly mimicked this feature by setting the bathymetry of the convergent part as:

$$262 \quad H(x, y) = H_{min} + (H_m - H_{min})\frac{y}{L} + (H_{max} - H_{min}) \times \left(1 - \frac{y}{L}\right) \left(1 - \frac{4x^2}{B^2}\right) e^{-C_f \left(\frac{4x^2}{B^2}\right)} \quad (2)$$

263 where L is the length of the convergent part (70 km); H_{max} (20 m) and H_{min} (3.0 m)
264 are the maximum and minimum water depths at the estuary mouth, the width-averaged
265 water depth H_m is constant ($H_m = 8$ m) along the estuary, and the parameter C_f is set
266 as 4, based on the bathymetry data. In the straight part of the estuary, the bathymetry
267 was kept the same as that of the uppermost cross-section of the convergent part.

268 At a distance of 75 km from the mouth of the main estuary, we added a sub-estuary
269 on the east side, resembling the East River sub-estuary. The sub-estuary extends in a
270 southwest-northeast direction for a distance of approximately 75 km. The width of the
271 sub-estuary is mildly convergent, with a width of 10 km at the confluence and
272 decreasing to 600 m at the head, with an e-folding decrease scale (L_b) of 90 km. The
273 water depth decreases landward from 6 m at the confluence to 3.5 m at the head of the
274 sub-estuary.

275 As the boundary conditions at an estuary mouth are generally unknown, we added
276 a continental shelf to the model domain. The shelf is 100 km wide and approximately
277 500 km long, with the downstream part (representing the Kelvin wave propagation
278 direction) being slightly longer than the upstream part. The water depth of the shelf is
279 uniform in the alongshore direction and increases linearly from the coast to the offshore
280 direction, with a slope of 1×10^{-4} . The model grid has 313×506 cells, with a cross-
281 channel spatial resolution of 300 m and an along-channel resolution of 500 m in the
282 estuary. The horizontal resolution decreases on the shelf and becomes 2 km at the open



283 ocean boundaries. Fifteen vertical s-grid layers were specified with higher resolutions
284 near the surface and bottom, and the coefficients of θ_s , θ_b , and h_c were set as 2.5,
285 3.0, and 5.0, respectively. In ROMS Model, coefficients larger than unity for θ_s , θ_b
286 can generate higher resolutions near the surface and bottom, respectively. For details of
287 these coefficients, the ROMS User manual can be referred to.

288 We used the $k - \varepsilon$ submodel of the Generic Length Scale (*GLS*) turbulence
289 closure scheme to calculate the vertical mixing (Umlauf and Burchard, 2003; Warner
290 et al., 2005). The horizontal eddy viscosity and diffusivity were calculated using the
291 Smagorinsky scheme (Smagorinsky, 1963). The bottom friction was calculated based
292 on the log-layer assumption near the bottom, with a bottom roughness length of 1 mm.
293 This setting results in a mean bottom drag coefficient of 0.005. The open ocean
294 boundary condition for the barotropic component consists of a Flather/Chapman
295 boundary condition for the depth-averaged flow and sea surface elevation (Chapman,
296 1985; Flather, 1976). The open boundary conditions for the temperature, salinity, and
297 baroclinic current are the Orlanski-type radiation conditions (Orlanski, 1976).

298 To investigate the impact of salt dynamics in the main estuary on salt intrusion in
299 the sub-estuary, two numerical experiments were implemented. In both cases, the river
300 discharge at the head of the sub-estuary was set as $200 \text{ m}^3/\text{s}$, which is approximately
301 the value during the dry season in 2021 in the East River estuary. A time series of water
302 levels produced by a combination of 12 tidal constituents was specified at the offshore
303 boundary. These 12 tidal constituents are M_2 , S_2 , N_2 , K_2 , K_1 ,
304 O_1 , P_1 , Q_1 , M_4 , MS_4 , M_m , M_f , respectively. The tidal constants of these 12
305 constituents were obtained from the Oregon Tidal Database (OPTS). As the tidal



306 amplitudes are almost doubled at the mouth of the main estuary due to the
307 superimposition of propagating and reflected tidal waves, the amplitudes of these tidal
308 constituents at the offshore boundary were reduced by half. Case 1 was set with a river
309 discharge of $1,500 \text{ m}^3 \text{ s}^{-1}$ at the main estuary's head. The river discharge of $1500 \text{ m}^3 / \text{s}$
310 is representative of the total amount that empties into the PRE from different outlets in
311 dry seasons (Gong et al., 2020), being lumped as input at the head of the PRE. The
312 inflowing river water was prescribed to have zero salinity and a temperature of 22°C ,
313 identical to the background temperature setting throughout the entire domain. The
314 incoming salinity at the offshore boundary was specified to be 34 psu. In Case 2, we
315 set an extremely low river discharge ($500 \text{ m}^3 \text{ s}^{-1}$) at the head of the main estuary, which
316 is realistic under the La Nina event. In this scenario, we aimed to check how the salt
317 dynamics in the more mixed main estuary affect the salinity variation in the sub-estuary.

318

319 **3.3 Analytical solutions for the salinity variation in the well-mixed sub-estuary**

320

321 For the subtidal (here is that averaged over 25 hours) salinity variation along the
322 well-mixed sub-estuary, the advection-diffusion equation can be written as:

$$323 \quad \frac{\partial(A\bar{S})}{\partial t} = -\frac{\partial}{\partial x}(A\bar{u}\bar{S}) + \frac{\partial}{\partial x}(AK_x \frac{\partial \bar{S}}{\partial x}) \quad (3)$$

324 where A is the cross-sectional area, \bar{S} is the subtidal salinity in the cross-section,
325 t is time, \bar{u} is subtidal longitudinal velocity, x is the distance along the sub-estuary,
326 K_x is the longitudinal dispersion coefficient. The left term in Eq. 3 indicates the local
327 acceleration and the unsteadiness of salinity variation. The unsteadiness is controlled
328 by the contrast between the internal and external timescales. The internal timescale of



329 the sub-estuary for a river discharge of 200 m³/s was estimated to be longer than 30
330 days. This timescale is longer than the fortnightly timescale, and the salinity in the sub-
331 estuary can hardly reach a steady state under the varying tides, thus the time tendency
332 term should not be ignored. However, when this term is included in the model, the
333 analytical solution of Eq. (3) becomes a little difficult to obtain as the horizontal
334 dispersion is time-dependent and varies with the tidal strength. We simplified this
335 problem by ignoring the unsteadiness term and assuming that the horizontal dispersion
336 is constant in a subtidal period and scales with the tidal current at the sub-estuary's
337 mouth. Meanwhile, the boundary condition of subtidal salinity at the sub-estuary's
338 mouth was updated at each subtidal period. In this way, the calculation of subtidal
339 salinity in the sub-estuary can be proceeded. As such, Eq. 3 becomes (Cai et al., 2015):

$$340 \quad \frac{Q}{A} \bar{S} = K_x \frac{\partial \bar{S}}{\partial x} \quad (4)$$

341 in which Q is the river discharge. We assume that the cross-sectional area decreases
342 exponentially in the landward, $A = A_0 \exp(-x/a)$, where a is the convergence
343 length scale of the cross-sectional area. When the longitudinal dispersion coefficient
344 K_x is assumed to be a constant along the sub-estuary, the subtidal salinity along the
345 sub-estuary can be obtained as:

$$346 \quad \frac{\bar{S}}{\bar{S}_0} = \exp\left\{-\frac{Qa}{A_0 K_x} \left[\exp\left(\frac{x}{a}\right) - 1\right]\right\} \quad (5)$$

347 For each subtidal period, we obtained the subtidal salinity (S_0) and the tidal current
348 at the mouth of the sub-estuary from the numerical model results, and related the
349 horizontal dispersion (K_x) to the tidal strength at the mouth. When these data were
350 available, the subtidal salinity at each subtidal period was calculated for our numerical
351 simulation period.



352 When the K_x is assumed to vary along the estuary, the salinity variation along the
353 sub-estuary is in another form and not presented here (Savenije, 2012), as that form of
354 K_x is not related to the tidal strength and is unsuitable for our situation here, so this
355 scenario is not pursued further.

356

357 **3.4 Calculation of the salt and freshwater fluxes**

358

359 The salt flux at a cross-section is calculated as follows:

$$360 \quad F_s = \int uSdA \quad (6)$$

361 where u is the instantaneous longitudinal velocity, and S is the instantaneous
362 salinity. The instantaneous flux was integrated and then averaged over a subtidal period
363 (25 hours).

364 As the changes in freshwater transport by the river-tide interaction are concerned,
365 we also calculated the freshwater flux, which is:

$$366 \quad F_f = \int u\left(1 - \frac{S}{S_0}\right)dA \quad (7)$$

367 where S_0 is the ocean salinity, here is taken to be 34 psu. The freshwater flux was
368 also integrated and averaged over a subtidal timescale.

369

370 **4. Results**

371

372 **4.1 The characteristics of salt dynamics in the sub-estuary: based on observation**

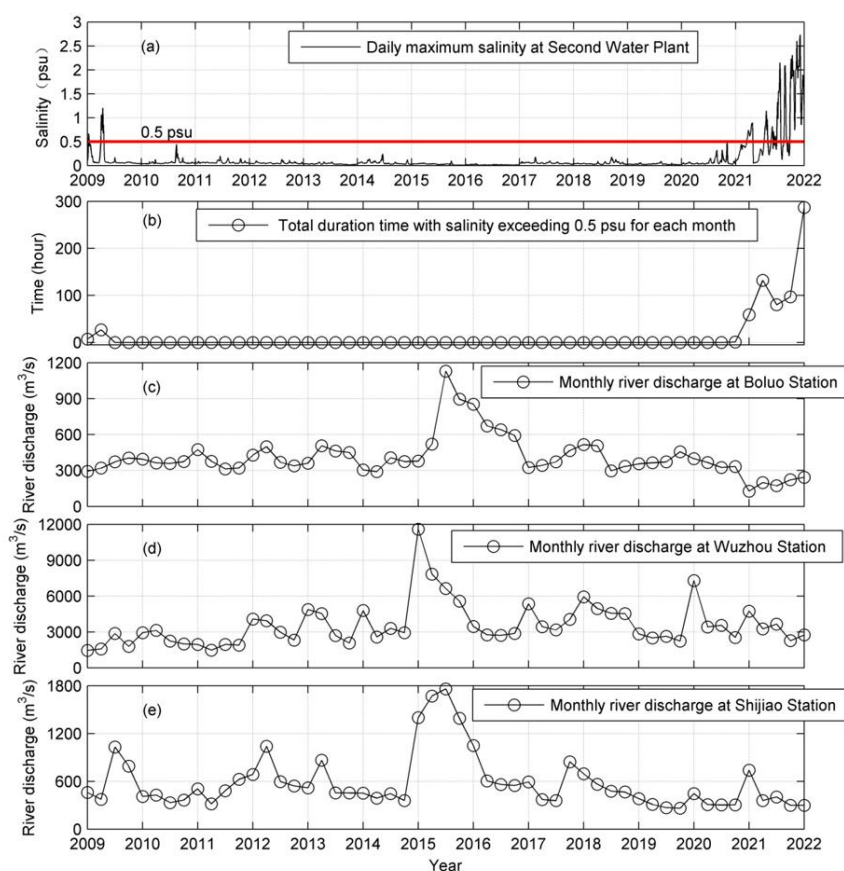
373 **data**

374

375 Here we take the Second Water Plant as a representative station in the upstream
376 region of the sub-estuary. The salinity variation at this station was checked from 2009
377 to 2022, as shown in Fig. 3. It indicates (Fig. 3a) that before 2021, the surface salinity



378 was generally lower than 0.5 psu and suitable for extraction. During the winter season
379 of 2021-2022, the salinity exceeded the drinking water criterion for a prolonged period
380 of 280 hours in January 2022 (Fig. 3b). These elevated salinities coincided with the
381 decreased river discharge from the upstream in the PRD, shown by the data at the
382 hydrological stations of Boluo, Wuzhou and Shijiao(Figs. 3c, 3d and 3e).

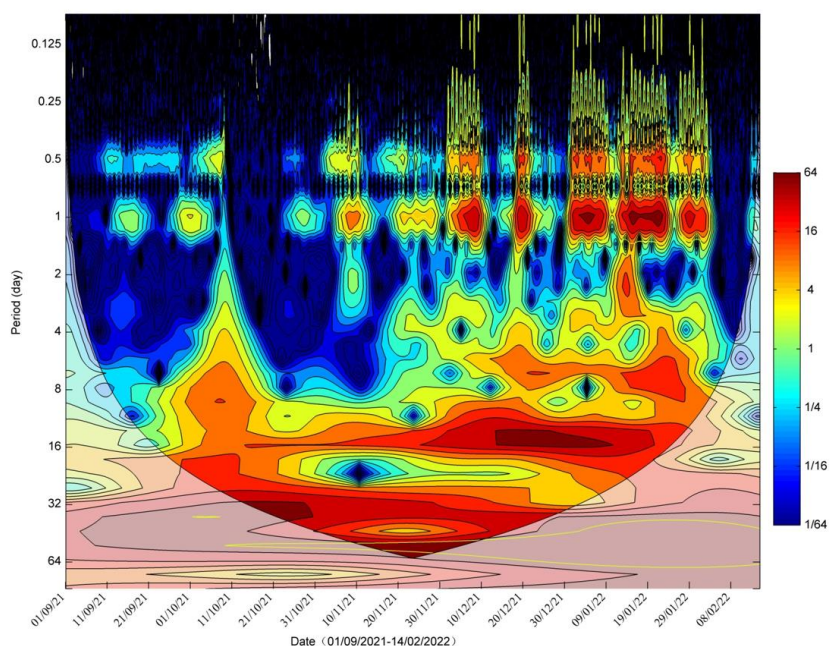


383
384 Fig.3. Timeseries of: a) Daily maximum salinity at the Second Water Plant; b) Total duration
385 period with salinity exceeding 0.5 psu for each month; c) Monthly river discharge at Boluo station
386 (upstream of the East River); d) Monthly river discharge at Wuzhou station (upstream of the West
387 River); e) Monthly river discharge at Shijiao station (upstream of the North River).



388

389 We conducted wavelet analysis for the salinity data of the Second Water Plant
390 Station from September 2021 to February 2022, when the salt intrusion was severe. The
391 result is shown in Fig. 4. It indicates that the power of salinity variations is concentrated
392 in several periods: one is in the range of 0.5 to 1 day, which is caused by tidal fluctuation;
393 the second period lies in the range of 5-9 days, which is presumably induced by wind
394 forcing; the third one is in the range of 14-16 days, obviously by the fortnightly
395 variation of spring-neap tidal cycle. The last one is within the range of 28 days, near
396 the monthly timescale. This periodicity should be caused by the tidal beating among
397 tidal constituents of M_2 , S_2 , N_2 , K_1 , O_1 , as indicated by Payo-Payo et al. (2022).



398

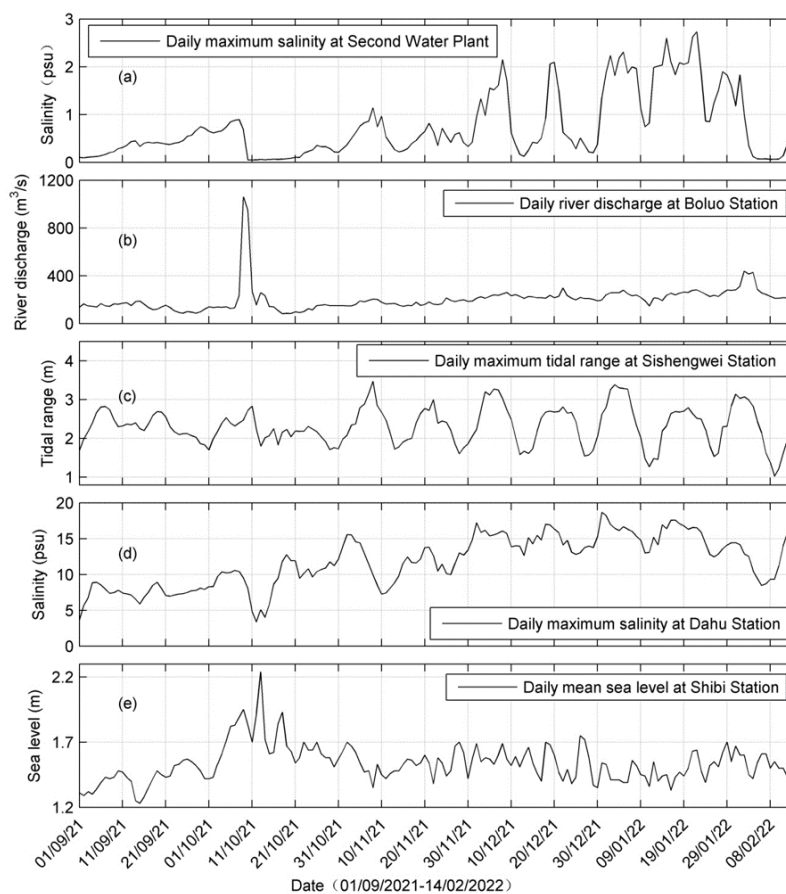
399

Fig. 4 Wavelet analysis of the salinity at the Second Water Plant

400



401 To identify the possible factors influencing the salinity variations in the sub-
402 estuary, we present the time series data of salinity at the Second Water Plant, river
403 discharge at Boluo station, tidal range at Sishengwei station, salinity at Dahu station
404 (located in the main estuary), and daily sea level at Shibi station (located at the mouth
405 of the main estuary) in Fig. 5. Firstly, it is evident that the variation of salinity at Dahu
406 (Fig. 5d) shows a consistent pattern with the changes in tidal range at Sishengwei (Fig.
407 5c), when the river discharge is relatively low after a flash flood event, which occurred
408 around October 21, 2021 (Fig. 5b). The highest salinity happened 2-3 days after neap
409 tides in the transition from neap to spring tides, whereas the lowest salinity occurred in
410 the transition from spring to neap tides, and generally occurred just before the neap
411 tides. This result indicates that the salinity and tidal range in the main estuary were
412 almost out of phase, and there existed a time lead of the salinity to the tidal range. This
413 pattern agrees well with what occurred in the Hudson River (Bowen and Geyer, 2003)
414 and the Modaomen Estuary (Gong and Shen, 2011), suggesting that the PRE remained
415 in a state of partially mixed. On the other hand, the salinity of the Second Water Plant
416 was almost in phase with the tidal range at the confluence (Fig. 5a vs. 5c). High
417 salinities coincided with spring tides, and low salinities occurred during neap tides. It
418 should be noted that the sea level at the PRE mouth showed a significant setup near
419 October 11, 2021, when a large increase in river discharge was observed in the PRD
420 due to a tropical storm (enumerated as the 17th typhoon in 2021, see the peak in Fig.
421 5b). This event caused a sharp decline in salinities at both Dahu and the Second Water
422 Plant, followed by a rebound approximately 10 days later.



423

424

425

426

427

428

429

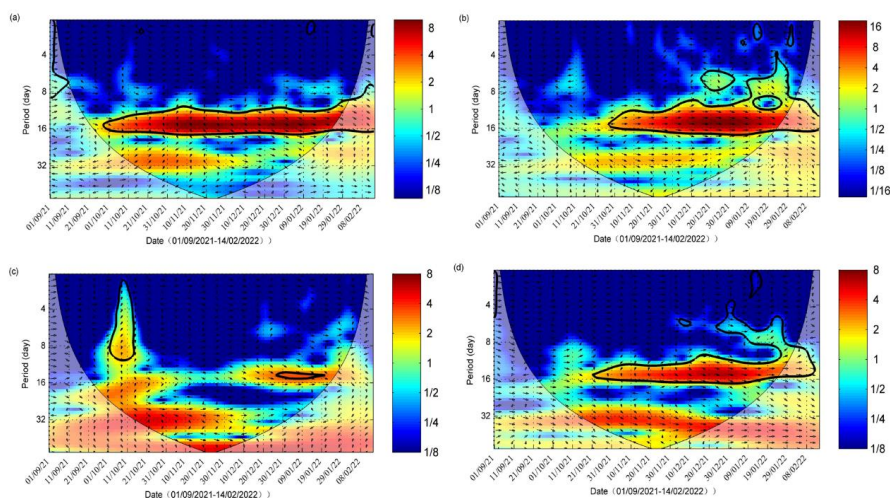
430

431

432

Fig. 5. Timeseries of: a) Daily maximum salinity at the Second Water Plant; b) Daily river discharge at Boluo station; c) Daily maximum tidal range at Sishengwei Station; d) Daily maximum salinity at Dahu Station; e) Daily mean sea level at Shibi Station.

The cross-wavelet analysis between salinity at Dahu and tidal range at Sishengwei (Figs. 6a) shows that the two variables are highly correlated in the periods of 14-16 days, indicating the effect of fortnightly spring-neap tidal variation. The arrow pointing down and right in this time band demonstrates that the change in tidal range lagged the variation of salinity.



433

434

Fig. 6. Cross-wavelet analysis of (a) between the salinity at Dahu and the tidal range at

435

Sishengwei; (b) between the salinity at the Second Water Plant and the tidal range at Sishengwei;

436

(c) between the salinity at the Second Water plant and the river discharge at the Boluo Station; (d)

437

between the salinity at the Second Water plant and that at the Dahu Station.

438

439

The cross-wavelet analysis between the salinity at the Second Water Plant and the

440

tidal range at Sishengwei station (Figs. 6b) shows that there existed a high common

441

power band of 14-16 days after October 21, 2021, and the phase relationship between

442

them was in phase, indicating that high salinities occurred during spring tides and low

443

salinities during neap tides, confirming the above results. It is also noted that before the

444

flood event on October 11, 2021, there was no high common power between these two

445

variables, even though the river discharge at the head of East River (Boluo Station) was

446

lower. This lack of high common power in the time band of 14-16 days before the

447

tropical storm event can also be noted in the cross-wavelet analysis between the salinity



448 at Dahu and the tidal range at Sishengwei. We also noted that before the storm event,
449 the water level at Sishengwei did not show distinct fortnightly spring-neap variations
450 (Fig. 5c). This lack of fortnightly cycle could be induced by the wind-induced
451 setup/setdown and/or the river-tide interaction, in which the river flow suppress the
452 tidal propagation. This phenomenon is peculiar and warrants a future study but beyond
453 the scope of this study.

454 The cross-wavelet analysis between the salinity at the Second Water Plant and the
455 river discharge at Boluo Station is presented in Fig. 6c. The high correlation during the
456 storm event was obvious, whereas, after that, the common power between the salinity
457 and river discharge was relatively low during the rebound period of the salinity at the
458 Second Water Plant. This low correlation could be due to the fact that the river discharge
459 did not change much and had no periodicity of 14-16 days then.

460 To examine the relationship between the salinities in the main estuary and at the
461 sub-estuary, we conducted a cross-wavelet analysis between the salinity at the Second
462 Water Plant and that at Dahu (Fig. 6d). There existed high common power between
463 these two variables in the time band of 14-16 days, the fortnightly tidal cycle. It also
464 shows that before October 21, 2021, the phase relationship between these two variables
465 was approximately in quadrature, indicating that the variation of the salinity at the
466 Second Water Plant lagged that at Dahu by 3.5-4 days. After October 21, 2021, the
467 phase relationship between them changed to in-phase when the river discharges in the
468 PRD became very low. This is quite interesting and will be explored in the following.

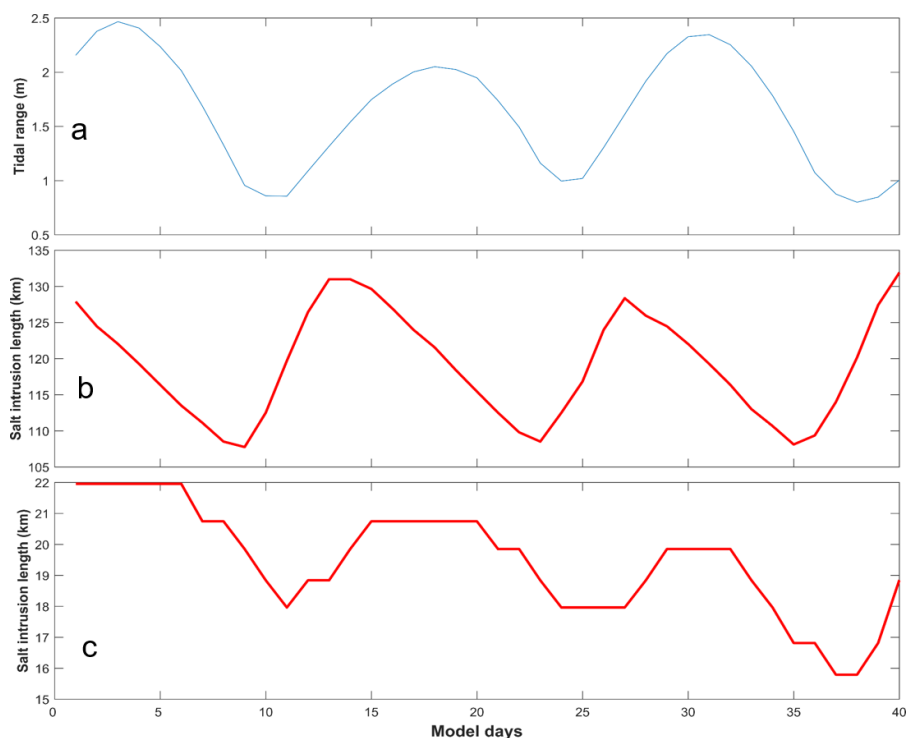
469



470 **4.2 The salt dynamics obtained through numerical simulations**

471

472 For Case 1 (base run), we intended to investigate the salt dynamics when the main
473 estuary stays in a state of partially mixed. Firstly we examine the variation of salt
474 intrusion length along the estuary's deep channel (Fig. 2b). Here the salt intrusion
475 length is defined as the distance of the bottom salinity isohaline of 5 psu from the
476 estuary mouth. It shows that the tidal range at the main estuary's mouth fluctuates at
477 fortnightly and monthly timescales. There occur two spring tides and neap tides in a
478 month (Fig. 7a), with one spring (neap) tide being stronger than the other one, as the
479 perigee/apogee cycle. The salt intrusion in the main estuary fluctuates with the tidal
480 range (Fig. 7b). The maximum salt intrusions occur just after neap tides, and the
481 minimum salt intrusions occur at the late of the transition from spring to neap tides,
482 consistent with the salinity change at the Dahu station shown above (Fig. 5d), and the
483 results we have demonstrated before (Gong et al., 2018). The relationship between the
484 salt intrusion and tidal range indicates an almost anti-phase one, suggesting that the
485 estuary is basically in a state of partially-mixed. This is because, for a partially-mixed
486 estuary, the landward salt transport is maximum during neap tides by the steady shear
487 and results in a maximum salt intrusion then. We present the tidally averaged
488 longitudinal profile of current and salinity for representative neap and spring tides in
489 Fig. S1 in the Supplement. The results confirm that during the neap tide, the estuary is
490 partially mixed, whereas, during the spring tide, the estuary becomes more mixed but
491 still in the state of partially mixed.



492

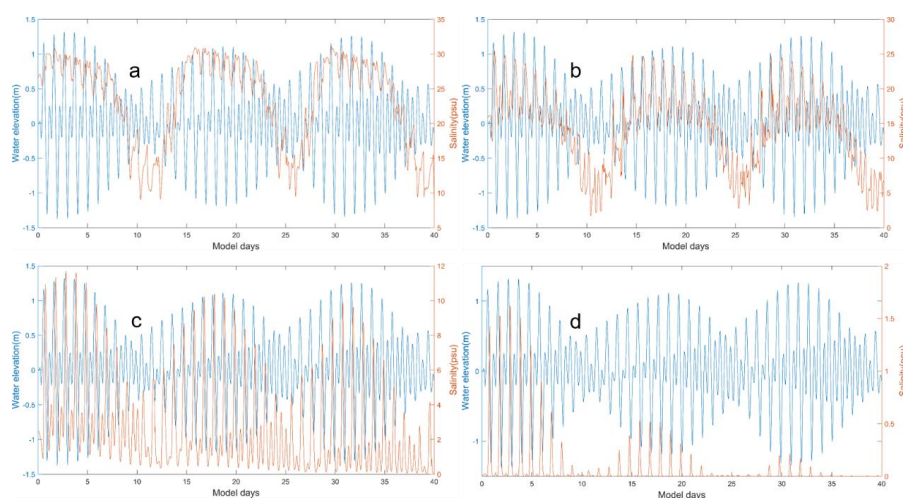
493 Fig. 7. Timeseries of: a) tidal range at the mouth of the main estuary; b) salt intrusion length along
494 the longitudinal section of the main estuary; c) salt intrusion length along the longitudinal section
495 of the sub-estuary.

496

497 We also checked the time series data of surface salinity and water level at a station
498 (S1, Fig. 2b) in the main estuary, roughly corresponding to the Dahu Station (Fig. 8a).
499 It shows that the surface salinity increases from neap to spring tides, and reaches
500 maxima before spring tides. It declines from the maxima to minima from spring to neap
501 tides, reaching the minima almost at neap tides. This shows that the salinity increases
502 faster from neap to spring than decreases from spring to neap. This asymmetry is also
503 noted in the variation of salt intrusion length, which increases sharply after the neap



504 tides but decreases more gradually from the maximum to the minimum. This
505 phenomenon has been discussed by Chen (2015) ; when the salt intrusion length is
506 shorter just before the neap tide, the acceleration by the net landward salt flux is stronger,
507 whereas when the salt intrusion length is longer, the deceleration of salt intrusion length
508 by net seaward salt flux is relatively weaker. The change in salinity leads that in tidal
509 range during spring tides but lags the tidal range during neap tides.



510
511 Fig. 8. Timeseries of water level at the confluence and surface salinity a) at S1 Station in the main
512 estuary; b) at S2 station (the confluence); c) at S3 station in the middle of the sub-estuary; d) at S4
513 station in the upstream region of the sub-estuary.

514
515 Similar to the analysis of observation data, we then investigate the salt intrusion
516 in the sub-estuary (Fig. 7c). Though the accuracy is not high, as our model resolution
517 in the sub-estuary is not fine enough, it clearly shows that the maximum salt intrusions
518 occur nearly in spring tides and the minimum salt intrusions in neap tides. This means
519 that the salt intrusion is in phase with the tidal range in the sub-estuary. We show the



520 tidally averaged profiles of current and salinity at the sub-estuary in Fig. S2 in the
521 Supplement. It indicates that the sub-estuary is mostly in a state of well-mixed during
522 both the neap and spring tides, though there appears some stratification near the mouth
523 of the sub-estuary during the neap tide. The 1 psu isohaline intrudes more in spring
524 tides than in neap tides. It should be noted that at the lower reach of the sub-estuary, the
525 surface salinity has a local high salinity zone (Fig. S2), consistent with the finding of
526 Haywood et al. (1982) at the lower York River in the Chesapeake Bay, USA.

527 To examine the salinity variations along the sub-estuary, we selected three stations
528 in the sub-estuary: one at the mouth (S2), one in the middle reach (S3), and the last one
529 in the upper reach (S4). The time series of water level at the confluence and salinities
530 at these three stations are shown in Figs. 8b, 8c and 8d. The salinity at the mouth of the
531 sub-estuary (Fig. 8b) fluctuates similarly to that in the main estuary: maximum salinities
532 occur right after neap tides and minimum salinities just before neap tides. In the middle
533 of the sub-estuary (Fig. 8c), the salinity variation almost keeps pace with that of the
534 tidal range: maximum salinities occur at spring tides and minimum salinities at neap
535 tides. At the upstream station, the salinity variation shows a similar pattern to that in
536 the middle of the sub-estuary. This indicates that when saline water propagates
537 upstream, it advances more landward and experiences less impedance during spring
538 tides and vice versa. We explore this phenomenon in the discussion part.

539

540 **4.3 The subtidal salt dynamics in the sub-estuary by the analytical solution**

541

542 We used the analytical solutions in Section 3.3 to explore the salt dynamics in the



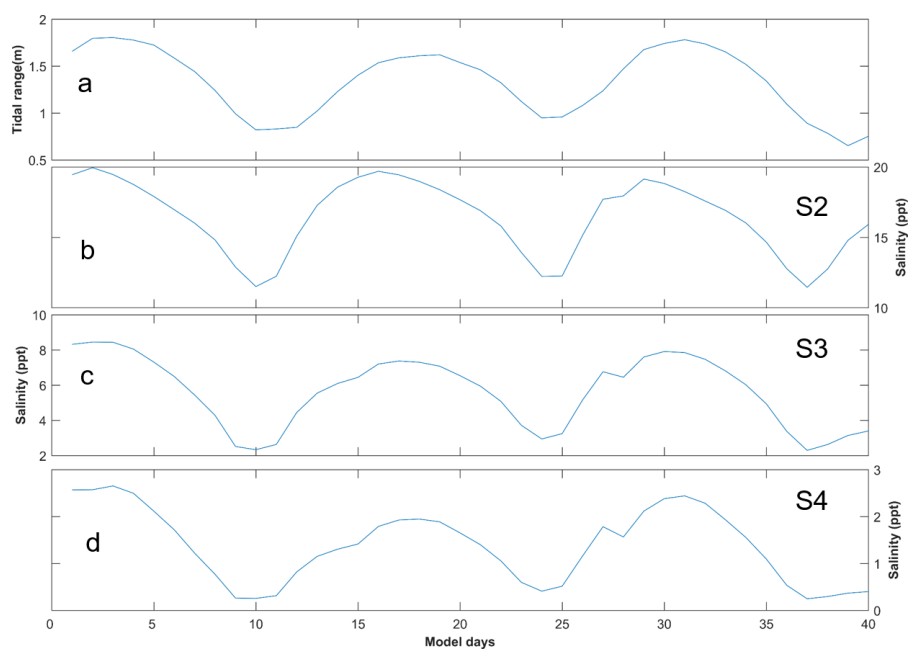
543 sub-estuary. In the sub-estuary, the exponential decaying constant of the cross-sectional
 544 area was calculated to be 50 km; and the river discharge was specified to be $200 \text{ m}^3 \text{ s}^{-1}$.
 545 ¹.

546 We used the scheme of constant dispersion along the sub-estuary, and the K_x was
 547 estimated as (Ralston et al., 2008):

$$548 \quad K_x = c_h \left(\frac{T_{tide}}{4} U_T \right) U_T \quad (8)$$

549 where c_h is an empirical constant of 0.0224, T_{tide} is the tidal period, here is set as
 550 12.42 hours; U_T is the tidal current amplitude at the sub-estuary's mouth.

551 We solved Eq. (5) for the model experiment Case 1. The results are shown in Fig.
 552 9.



553
 554 Fig. 9. The results of the analytical solution of salinity variations along the sub-estuary. a)
 555 tidal range at the mouth of the sub-estuary; b), c), and d) are subtidal salinity variations at S2,
 556 S3, and S4 stations.



557

558 Under the $1500 \text{ m}^3 \text{ s}^{-1}$ river discharge at the head of the main estuary, the tidal
559 range at the sub-estuary's mouth varies between spring and neap tides, with a greater
560 spring and a weaker spring in a month (Fig. 9a). The subtidal salinity at the confluence
561 (S2 station, Fig. 9b) varies between 10 and 20 psu, with the maximum salinities
562 occurring before the spring tides and the minimum salinities before the neap tides,
563 indicating a phase lead of salinity to the tidal range. In the middle of the sub-estuary
564 (S3 station, Fig. 9c), the salinity fluctuates between 2 and 10 psu, and there exists a
565 slight phase lead of salinity to that of the tidal range. In the upstream region of the sub-
566 estuary (S4 station, Fig. 9d), the salinity fluctuates between 0 and 3 psu, and the salinity
567 variation becomes almost in phase with that of the tidal range at the confluence.
568 Compared to the numerical simulation results, the analytical solution reproduces the
569 trend of the phase relationship between the salinity and tidal range along the sub-estuary:
570 the phase of the salinity variation leads that of the tidal range at the sub-estuary's mouth
571 and becomes more in phase with that of the tidal range in the middle and upstream
572 region of the sub-estuary. Meanwhile, the fluctuation magnitude in the middle of the
573 sub-estuary is well reproduced. However, the fluctuation range in the upstream region
574 of the sub-estuary is over-estimated, showing the weakness of assuming a uniform
575 horizontal dispersion along the sub-estuary.

576

577 **5. Discussion**

578

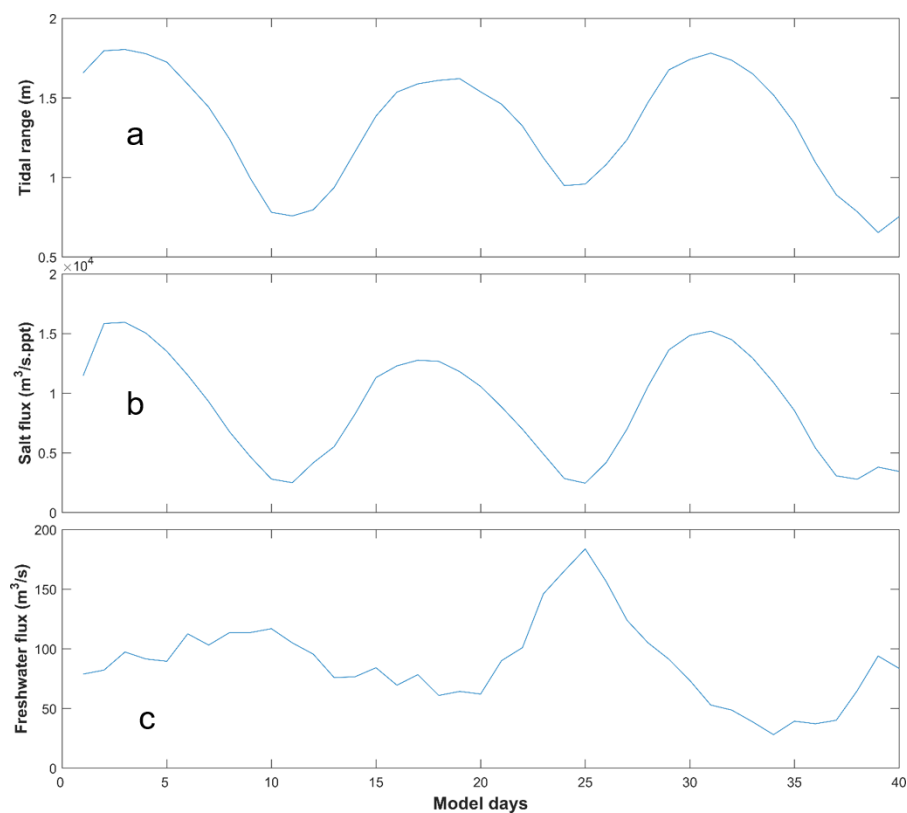
579 **5.1 The physics behind the change in phase relationship between the salinity and** 580 **tidal range along the sub-estuary**

581

582 The numerical results and analytical solutions both indicate that near the sub-
583 estuary's mouth, the salinity fluctuation leads that of the tidal range, and in the middle
584 and upstream region of the sub-estuary, the salinity variation becomes more in phase



585 with that of the tidal range. The analytical solution shows that the changes in the phase
586 relationship between these two variables are mostly caused by the change in horizontal
587 dispersion, that is, the larger dispersions during spring tides cause increased landward
588 salt transport, resulting in elevated salinity in the middle and upstream regions of the
589 sub-estuary. The results of numerical simulation are a combination of many
590 interweaved processes and a little harder to interpret. To unravel the physics in the
591 numerical simulation, we examine the salt transport in the lower reach at a cross-section
592 near the sub-estuary mouth and freshwater transport in the upstream cross-section of
593 the sub-estuary (shown in Fig. 2b).



594

595

Fig. 10. Timeseries of: a) tidal range at the mouth of the sub-estuary; b) salt flux at the



596 cross-section near the mouth of the sub-estuary; c) freshwater flux at the cross-section in the
597 upstream region of the sub-estuary. It should be noted that the freshwater flux is the magnitude
598 and has a sign opposite to the salt flux.

599

600 The results are shown in Fig. 10. From Fig. 10b, the subtidal salt flux near the sub-
601 estuary's mouth is always landward in the simulation period and is higher during spring
602 tides and lower during neap tides. The change in salt flux leads that of the tidal range,
603 consistent with the phase relationship between salinity and tidal range near the sub-
604 estuary's mouth (Fig. 8b). As the sub-estuary is well-mixed during the simulation
605 period, the landward salt transport is mostly induced by the tidal oscillatory transport
606 and justifies ignoring the steady shear part in Eq. (3). The subtidal freshwater flux in
607 the upstream region of the sub-estuary is seaward, and shows a pattern that larger
608 freshwater fluxes occur during neap tides and smaller freshwater fluxes during spring
609 tides (Fig. 10c). This pattern has been well studied by Buschman et al. (2009) in the
610 subtidal momentum dynamics. They showed that the primary subtidal momentum
611 balance is between the water level gradient and bottom friction. During spring tides,
612 the subtidal bottom friction is larger and the subtidal water slope is greater, meaning
613 that more freshwater is being detained upstream to elevate the water level there. During
614 neap tides, the detained freshwater in the upstream is released downstream and results
615 in increased freshwater fluxes. In this way, the saline water from the sub-estuary's
616 mouth experiences less impedance and dilution during spring tides and thus advances
617 more landward, resulting in an enhanced salt intrusion during spring tides, and vice



618 versa. The above results indicate that the more in-phase relationship between the
619 salinity and tidal range in the middle and upstream region of the sub-estuary is mostly
620 generated by the fortnightly variation of the tidal strength and the associated variations
621 of horizontal dispersion and freshwater flux by the river-tide interaction. The larger the
622 dispersion, the more salt is pumped into the upstream. The stronger the tidal strength,
623 the more freshwater is detained upstream and less impedance to the salt intrusion.

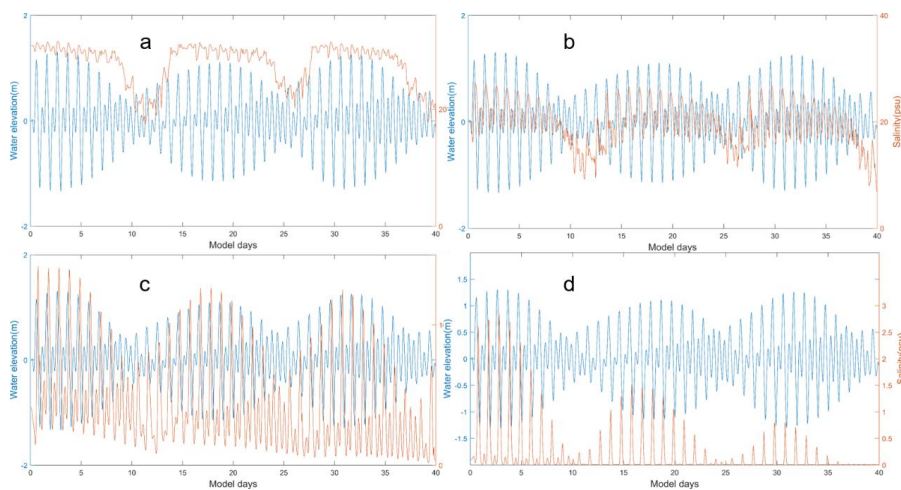
624 From the above results, it is seen that the salinity dynamics in the sub-estuary show
625 a pattern that is more influenced by the main estuary in the lower reach and becomes
626 more controlled by internal tidal processes in the middle and upstream regions of the
627 sub-estuary.

628

629 **5.2 How do the salt dynamics in the main estuary affect that in the sub-estuary?**

630

631 To further study how the changes in salinity dynamics in the main estuary affect
632 the salinity variation in the sub-estuary, we set up another experiment. In the model
633 scenario of Case 2, we set an extremely low river discharge ($500 \text{ m}^3 \text{ s}^{-1}$) at the head of
634 the main estuary, and the results are shown in Fig. 11. Simultaneously, the analytical
635 solutions for the scenario of Case 2 are presented in Fig. 12.



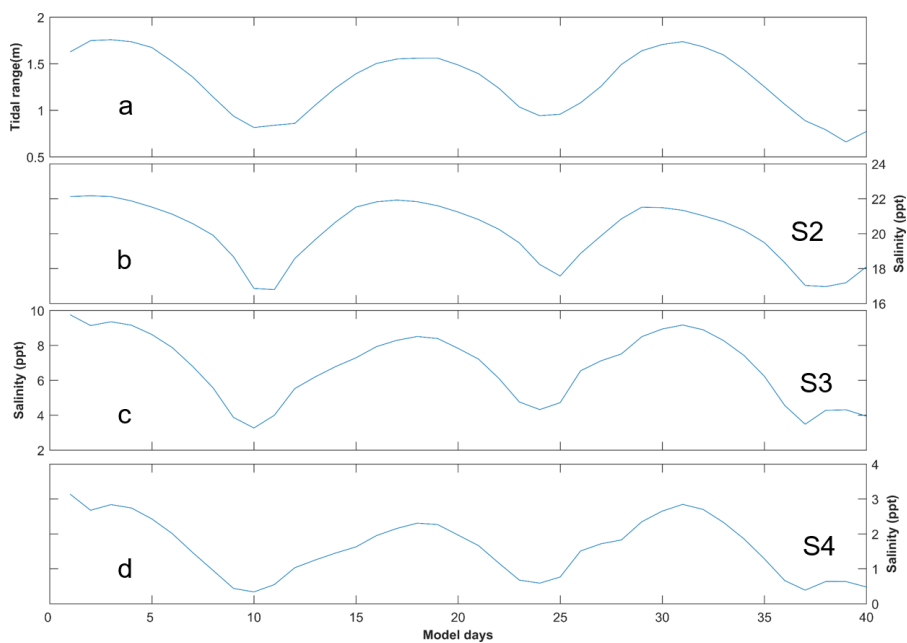
636

637

638

639

Fig. 11. Timeseries of water level at the confluence and surface salinity under the extremely lower river discharge in the main estuary at stations of: a) S1; b) S2; c) S3; d) S4.



640

641

642

Fig. 12. The results of the analytical solution of salinity variations along the sub-estuary under extremely dry conditions. a) tidal range at the mouth of the sub-estuary; b), c), and d) are



643 subtidal salinity variations at S2, S3, and S4 stations.

644

645 With decreased river discharge from the head of the main estuary, the salt intrusion
646 front is shifted more landward. The S1 station is now located in the polyhaline region
647 with a mean salinity of approximately 26 psu (Fig. 11a). The minimum salinities
648 coincide more with neap tides but the maximum salinities occur around spring tides.
649 The asymmetry between salinity rise and fall is decreased, with salinities jumping
650 quickly after neap tides, keeping elevated around spring tides, and dropping quickly
651 just before neap tides. For the intratidal variation, it can be seen that during a tidal cycle,
652 the salinity fluctuation is reduced when compared to Case 1 (Figs. 11a vs 8a), which is
653 mostly due to the fact that with the reduced river discharge, the salinity gradient in the
654 polyhaline reach of the main estuary is decreased.

655 For the S2 Station (at the confluence, Figs. 11b and 12b), it is now located in the
656 mesohaline region, with the salinity ranging from 5 to 26 psu. The highest and lowest
657 salinities are both increased when compared to Case 1, with a reduced magnitude of
658 salinity change in a tidal cycle. The salinity variation pattern remains similar to that in
659 Case 1, with minimum salinities occurring just before neap tides, and maximum
660 salinities after neap tides, but occur closer to spring tides. The asymmetry of quick
661 increase from neap to spring but gradual decrease afterwards is still clear.

662 When entering into the sub-estuary, the salinity variation at S3 in the middle of the
663 sub-estuary shows a more in-phase relationship between salinity and tidal range (Figs.
664 11c and 12c). The maximum salinities occur closer to spring tides whereas the



665 minimum salinities still occur just before neap tides. In the upstream region of the sub-
666 estuary (Figs. 11d and 12d), the phase relationship between salinity and tidal range is
667 also an in-phase one. Combined with the situation at the S1 Station, it indicates that the
668 variations of salinity at stations S4 and S1 are more synchronous. This largely explains
669 the observed phenomenon that under more drought conditions, the salinity variations at
670 the Second Water Plant kept pace with those at the Dahu Station (Section 3.1).

671

672 **5.3 Limitations and implications of this study**

673

674 In this study, we focus on the phase relationship between the variations of salinity
675 and tidal range, both in a sub-estuary and the main estuary. The salinity variations along
676 the sub-estuary are revealed to be associated with the salinity dynamics in the main
677 estuary, linked by the salinity variations at the confluence between the main estuary and
678 the sub-estuary. In a spring-neap tidal cycle, even when the salinity at the confluence is
679 a little lower during the spring tide than that during the neap tide, the higher horizontal
680 dispersion and decreased freshwater release at the head of the sub-estuary during the
681 spring tide can pump more saline water from the confluence into the middle and
682 upstream of the sub-estuary, and cause the salinities there to be higher than during the
683 neap tide. In this way, the salinity variations at areas farther away from the confluence
684 become more synchronous with the tidal range.

685 However, this study did not consider the effect of winds and waves, as shown to
686 be important in previous studies such as Gong et al. (2018). The variations of salinity
687 in the period of 5-8 days should be related to the wind effects and await future



688 exploration. The effect of sea level change outside the main estuary was also not
689 examined in detail, though it can be intrinsically linked to the effect of winds and waves.
690 Finally, we did not explore a full parameter space of river discharge, tidal range, and
691 bathymetry situations, and thus can not give a synthesis of the sub-estuary salt intrusion
692 dynamics at this time.

693 Despite all these limitations, this study has implications for studying salt intrusion
694 dynamics in sub-estuaries, which are influenced by both the hydrodynamics inside the
695 sub-estuary and the salt dynamics in the main estuaries. It is also of importance for
696 providing a scientific basis for salt intrusion mitigation in the region. For example, salt
697 intrusion in the sub-estuary is not only impacted by the river discharge from the head
698 of the sub-estuary itself but also largely affected by the salt dynamics in the main estuary.
699 In this respect, apart from releasing more freshwater from the upstream in the sub-
700 estuary, measures to control the salinity variations at the confluence between the main
701 estuary and the sub-estuary also need to be taken into consideration. This may involve
702 implementing engineering solutions such as the construction of barriers or gates to
703 regulate the inflow of saltwater from the main estuary into the sub-estuary. Additionally,
704 the management of water withdrawals and releases in the sub-estuary and main estuary
705 needs to be optimized by taking the estuarine system as a whole. Overall, a
706 comprehensive and coordinated approach is necessary to effectively mitigate salt
707 intrusion in sub-estuaries.

708

709 **6. Summary and conclusions**

710



711 From 2021 to 2022, under the influence of an extended La Nina event, the Pearl
712 River Delta region in China experienced a prolonged extreme drought condition, and
713 the sub-estuary (East River estuary) also suffered greatly from the enhanced salt
714 intrusion. To identify the characteristics of the salt intrusion in the sub-estuary, and to
715 explore the underlying physics in controlling the spatio-temporal variations of the salt
716 intrusion, we collected observation data and conducted numerical simulations for
717 idealized estuarine bathymetry, and used analytical solutions for the subtidal salinity
718 variations in the sub-estuary. The observation data showed that the salinity variation in
719 the main estuary usually led that of the tidal range, and the asymmetry between salinity
720 rise and fall in a fortnightly timescale was prominent. However, in the upstream region
721 of the sub-estuary, the salinity variation was in phase with that of the tidal range, and
722 the salinity rise and fall were more symmetrical. The idealized model simulations and
723 the analytical solution both reproduced these phenomena.

724 We note that under drought conditions, the river-tide interaction played a role in
725 the in-phase relationship between the salinity and tidal range upstream region of the
726 sub-estuary. The salinity variation in the middle and upstream regions of the sub-
727 estuary can keep pace with that of the tidal range. The analytical results show that the
728 horizontal dispersion scaling with tidal strength can largely reproduce the changes in
729 phase relationship between salinity and tidal range in the sub-estuary. We conclude that
730 both the changes in horizontal dispersion and the river-tide interaction in modulating
731 the freshwater release are responsible for the in-phase relationship between the salinity
732 and tidal range in the middle and upstream regions of the sub-estuary.



733 This study is of help in the investigation of salt dynamics in sub-estuaries
734 connected to main estuaries, and of implications for mitigating salt intrusion problems
735 in the regions suffered from enhanced salt intrusion by climate change and human
736 interventions.

737

738 **Data availability:** The observation data can be downloaded from the website
739 <http://www.pearlwater.gov.cn/>. The numerical data is available upon request to the
740 corresponding author.

741

742 **Declaration of competing interest**

743 The contact author has declared that none of the authors has any competing
744 interests.

745

746 **CRedit authorship contribution statement**

747 **Zhongyuan Lin:** Data collection, wavelet analysis, Writing - original draft, Writing -
748 review & editing. **Guang Zhang:** numerical modeling, Writing - review & editing.

749 **Huazhi Zou:** Writing-review & editing, funding acquisition. **Wenping Gong:**
750 Conceptualization, Methodology, Writing-review & editing, funding acquisition.

751

752 **Acknowledgments**

753

754 This research was funded by the National Natural Science Foundation of China
755 (grant numbers 42276169, 42306015) and The Science and Technology Innovation



756 Program from Water Resources of Guangdong Province (2023-01).

757

758 **Supplement:**

759

760 We present the longitudinal profiles of subtidal current and salinity along the
761 channels in the main estuary and the sub-estuary during typical spring and neap tides.
762 Fig. S1 is for the dry condition with 1500 m³/s at the head of the main estuary, and Fig.
763 S2 for the extremely dry condition with 500 m³/s released at the head of the main estuary.

764

765 **References**

766

767 Bowden, K. F., 1965. Horizontal mixing in the sea due to a shearing current. *Journal of*
768 *Fluid Mechanics* 21, 83-95. <https://doi.org/10.1007/BF00167972>

769 Bowen, M., Geyer, W.R., 2003. Salt transport and the time-dependent salt balance of a
770 partially stratified estuary. *Journal of Geophysical Research* 108(C5), 3185.
771 Doi:10.1029/2001JC001231.

772 Buschman, F. A., Hoitink, A. J. F., Vejt., M. V. D., 2009. Subtidal water level variation
773 controlled by river flow and tides. *Water Resources Research* 45(10), W10420.
774 <https://doi.org/10.1029/2009WR008167>

775 Cai, H., Savenije, H.H.G., Zuo, S., Jiang, C., Chua, V.P., 2015. A predictive model for
776 salt intrusion in estuaries applied to the Yangtze estuary. *Journal of Hydrology* 529,
777 1336-1349.

778 Chapman, D. C., 1985. Numerical Treatment of Cross-Shelf Open Boundaries in a
779 Barotropic Coastal Ocean Model. *Journal of Physical Oceanography* 15(8), 1060-
780 1075.



- 781 Chen S.-N., 2015. Asymmetric Estuarine Responses to Changes in River Forcing: A
782 Consequence of Nonlinear Salt Flux. *Journal of Physical Oceanography* 45(11),
783 2836-2847. <https://doi.org/10.1175/JPO-D-15-0085.1>
- 784 Dong, L., Su, J., Wong, L., Cao, Z., Chen, J.-C., 2004. Seasonal variation and dynamics
785 of the Pearl River plume. *Continental Shelf Research* 24(16), 1761-1777.
786 <https://doi.org/10.1016/j.csr.2004.06.006>
- 787 Flather, R. A., 1976. A tidal model of the northwest European continental shelf, A tidal
788 model of the northwest European continental shelf. *Mem. Soc. R. Sci. Liege* 10(6),
789 141-164.
- 790 Gong, W., Shen, J., 2011. The response of salt intrusion to changes in river discharge
791 and tidal mixing during the dry season in the Modaomen Estuary, China.
792 *Continental Shelf Research*, 31, 769–788.
- 793 Gong, W., Lin, Z., Chen, Y., Chen, Z., Zhang, H., 2018. Effect of winds and waves on
794 salt intrusion in the Pearl River estuary. *Ocean Science* 14(1), 139-159.
795 <https://doi.org/10.5194/os-14-139-2018>
- 796 Gong, W., Chen, L., Zhang, H., Yuan, L., Chen, Z., 2020. Plume Dynamics of a Lateral
797 River Tributary Influenced by River Discharge From the Estuary Head. *Journal of*
798 *Geophysical Research: Oceans*. doi: 10.1029/2019JC015580.
- 799 Gong, W., Lin, Z., Zhang, H., Lin H., 2022. The response of salt intrusion to changes
800 in river discharge, tidal range, and winds, based on wavelet analysis in the
801 Modaomen estuary, China. *Ocean & Coastal Management* 219, 106060.
802 <https://doi.org/10.1016/j.ocecoaman.2022.106060>



- 803 Haidvogel, D. B., Arango, H. G., Hedstrom, K., Beckmann, A., Malanotte-Rizzoli, B.,
804 Shchepetkin, A. F., 2000. Model evaluation experiments in the North Atlantic
805 Basin: Simulations in nonlinear terrain-following coordinates. *Dynamics of*
806 *Atmospheres and Oceans* 32(3-4), 239-281. [https://doi.org/10.1016/S0377-](https://doi.org/10.1016/S0377-0265(00)00049-X)
807 [0265\(00\)00049-X](https://doi.org/10.1016/S0377-0265(00)00049-X)
- 808 Haywood, D., Welch, C. S., Hass, L. W., 1982. York River destratification: an estuary-
809 sub-estuary interaction. *Science* 216, 1413-1414.
810 <https://doi.org/10.1126/science.216.4553.1413>
- 811 Hong, B., Liu, Z., Shen, J., Wu, H., Gong, W., Xu, H., Wang, D., 2020. Potential
812 physical impacts of sea-level rise on the Pearl River Estuary, China. *Journal of*
813 *Marine Systems* 201, 103245. <https://doi.org/10.1016/j.jmarsys.2019.103245>
- 814 Hu, J., Li, S., Geng, B., 2011. Modeling the mass flux budgets of water and suspended
815 sediments for the river network and estuary in the Pearl River Delta, China. *Journal*
816 *of Marine Systems* 88(2), 252-266. <https://doi.org/10.1016/j.jmarsys.2011.05.002>
- 817 Jia, L., Luo, Z., Yang, Q., Ou, S., Lei, Y., 2006. The impact of massive sand mining on
818 the morphology and tidal dynamics in the downstream of East River and the East
819 River Delta (In Chinese). *Acta Geographica Sinica* 2006(09), 985-994.
- 820 Liu, B., Yan, S., Chen, X., Lian, Y., Xin, Y., 2014. Wavelet analysis of the dynamic
821 characteristics of saltwater intrusion - A case study in the Pearl River Estuary of
822 China. *Ocean & Coastal Management* 95, 81-92.
823 <https://doi.org/10.1016/j.ocecoaman.2014.03.027>
- 824 MacCready, P., Geyer, W. R., 2010. Advances in estuarine physics. *Annual Review of*



- 825 Marine Science 2(1), 35–58. <https://doi.org/10.1146/annurev-marine-120308->
826 081015.
- 827 Mao, Q., Shi, P., Yin, K., Gan, J., Qi, Y., 2004. Tides and tidal currents in the Pearl River
828 Estuary. Continental Shelf Research 24(16), 1797-1808.
829 <https://doi.org/10.1016/j.csr.2004.06.008>
- 830 Okubo, A., 1973. Effect of shoreline irregularities on streamwise dispersion in estuaries
831 and other embayments. Netherlands Journal of Sea Research 6, 213-224.
832 [https://doi.org/10.1016/0077-7579\(73\)90014-8](https://doi.org/10.1016/0077-7579(73)90014-8)
- 833 Orlandi, I., 1976. A simple boundary condition for unbounded hyperbolic flows.
834 Journal of Computational Physics 21(3), 251–269.
835 [http://dx.doi.org/10.1016/0021-9991\(76\)90023-1](http://dx.doi.org/10.1016/0021-9991(76)90023-1)
- 836 Payo-Payo, M., Bricheno, L. M., Dijkstra, Y. M., Cheng, W., Gong, W., Amoudry, L.
837 O., 2022. Multiscale temporal response of salt intrusion to transient river and
838 ocean forcing. Journal of Geophysical Research: Oceans 127, e2021JC017523.
839 <https://doi.org/10.1029/2021JC017523>.
- 840 Ralston, D. K., Geyer, W. R., Lerczak J. A., 2010. Structure, variability, and salt flux in
841 a strongly forced salt wedge estuary, J. Geophys. Res., 115, C06005,
842 doi:10.1029/2009JC005806.
- 843 Ralston, D. K., Geyer, W. R., 2019. Response to channel deepening of the salinity
844 intrusion, estuarine circulation, and stratification in an urbanized estuary. Journal
845 of Geophysical Research: Oceans 124, 4784–4802.
846 <https://doi.org/10.1029/2019JC015006>



- 847 Savenije, H.H.G., 2012. Salinity and tides in alluvial estuaries. Second Edition
848 <www.salinityandtides.com>.
- 849 Simpson, J.H., Brown, J., Matthews, J.P., Allen, G., 1990. Tidal straining, density
850 currents, and stirring in the control of estuarine stratification. *Estuaries* 13 (2),
851 125–132.
- 852 Smagorinsky, J., 1963. General Circulation Experiments with the Primitive Equation,
853 Part 1, the Basic Experiment. *Monthly Weather Review* 91(3), 99-164.
854 <http://dx.doi.org/10.1175/1520-0493>
- 855 Spinoni, J., Naumann, G., Carrao, H., Barbosa, P., Vogt, J., 2014. World drought
856 frequency, duration, and severity for 1951–2010. *Int. J. Climatol.* 34, 2792–2804.
- 857 Stommel, H., Farmer, H. G., 1952. On the nature of estuarine circulation: part I
858 (chapters 3 and 4). Woods Hole Oceanographic Institution.
- 859 Umlauf, L., Burchard, H., 2003. A generic length-scale equation for geophysical
860 turbulence models. *Journal of Marine Research* 61(2), 235-365.
861 <https://doi.org/10.1357/002224003322005087>
- 862 Uncles, R. J., Stephens, J. A., 2010. Turbidity and sediment transport in a muddy sub-
863 estuary. *Estuarine, Coastal and Shelf Science* 87(2), 213-224.
864 <https://doi.org/10.1016/j.ecss.2009.03.041>
- 865 Warner, J. C., Sherwood, C. R., Arango, H. G., Signell, R. P., Butman, B., 2005.
866 Performance of four turbulence closure models implemented using a generic length
867 scale method. *Ocean Modeling* 8, 81–113.
- 868 Wong, L. A., Chen, J. C., Xue, H., Dong, L. X., Su, J. L., Heinke, G., 2003. A model



869 study of the circulation in the Pearl River Estuary (PRE) and its adjacent coastal
870 waters: 1. Simulations and comparison with observations. *Journal of Geophysical*
871 *Research* 108(C5). <https://doi.org/10.1029/2002jc001451>

872 Wu, Z. Y., Saito, Y., Zhao, D. N., Zhou, J. Q., Cao, Z. Y., Li, S. J., 2016. Impact of
873 human activities on subaqueous topographic change in Lingding Bay of the Pearl
874 River estuary, China, during 1955-2013. *Scientific Reports* 6, 37742.
875 <https://doi.org/10.1038/srep37742>

876 Yellen, B., Woodruff, J. D., Ralston, D. K., MacDonald, D. G., Jones, D. S., 2017. Salt
877 wedge dynamics lead to enhanced sediment trapping within side embayments in
878 high-energy estuaries. *Journal of Geophysical Research: Oceans* 122(3), 2226-
879 2242. <https://doi.org/10.1002/2016JC012595>

880 Zhang, P., Yang, Q., Wang, H., Cai, H., Liu, F., Zhao, T., Jia, L., 2021. Stepwise
881 alterations in tidal hydrodynamics in a highly human-modified estuary: The roles
882 of channel deepening and narrowing. *Journal of Hydrology* 597, 126153.

883 Zimmerman, J. T. F., 1986. The tidal whirlpool: A review of horizontal dispersion by
884 tidal and residual currents. *Netherlands Journal of Sea Research* 20, 133-154.
885 [https://doi.org/10.1016/0077-7579\(86\)90037-2](https://doi.org/10.1016/0077-7579(86)90037-2)
886



887

888 **Figure Captions:**

889

890 Fig.1. a) The East River estuary; b) Map of the Pearl River Delta and the
891 locations of hydrological and water level stations.

892 Fig. 2. Geometry and bathymetry of the idealized model domain: a)for the
893 whole domain; b)zoom in for the area of concern. The origin of the coordinates is in
894 the middle of the main estuary mouth. The longitudinal sections in the main and sub-
895 estuary are shown as dashed lines, and the cross-sections inside the sub-estuary are
896 shown as color solid lines. The locations of several stations are indicated.

897 Fig.3. Timeseries of: a) Daily maximum salinity at the Second Water Plant; b)
898 Total duration period with salinity exceeding 0.5 psu for each month; c) Monthly
899 river discharge at Boluo station (upstream of the East River); d) Monthly river
900 discharge at Wuzhou station (upstream of the West River); e) Monthly river discharge
901 at Shijiao station (upstream of the North River).

902 Fig. 4 Wavelet analysis of the salinity at the Second Water Plant.

903 Fig. 5. Timeseries of: a) Daily maximum salinity at the Second Water Plant; b)
904 Daily river discharge at Boluo station; c) Daily maximum tidal range at Sishengwei
905 Station; d) Daily maximum salinity at Dahu Station; e) Daily mean sea level at Shibi
906 Station.

907 Fig. 6. Cross-wavelet analysis of (a) between the salinity at Dahu and the tidal
908 range at Sishengwei; (b) between the salinity at the Second Water Plant and the tidal
909 range at Sishengwei; (c) between the salinity at the Second Water plant and the river



910 discharge at the Boluo Station; (d) between the salinity at the Second Water plant and
911 that at the Dahu Station.

912 Fig. 7. Timeseries of: a) tidal range at the mouth of the main estuary; b) salt
913 intrusion length along the longitudinal section of the main estuary; c) salt intrusion
914 length along the longitudinal section of the sub-estuary.

915 Fig. 8. Timeseries of water level at the confluence and surface salinity a) at S1
916 Station in the main estuary; b) at S2 station (the confluence); c) at S3 station in the
917 middle of the sub-estuary; d) at S4 station in the upstream region of the sub-estuary.

918 Fig. 9. The results of the analytical solution of salinity variations along the sub-
919 estuary. a) tidal range at the mouth of the sub-estuary; b), c), and d) are subtidal
920 salinity variations at S2, S3, and S4 stations.

921 Fig. 10. Timeseries of: a) tidal range at the mouth of the sub-estuary; b) salt flux
922 at the cross-section near the mouth of the sub-estuary; c) freshwater flux at the cross-
923 section in the upstream region of the sub-estuary.

924 Fig. 11. Timeseries of water level at the confluence and surface salinity under
925 the extremely lower river discharge in the main estuary at stations of: a) S1; b) S2; c)
926 S3; d) S4.

927 Fig. 12. The results of the analytical solution of salinity variations along the sub-estuary
928 under extremely dry conditions. a) tidal range at the mouth of the sub-estuary; b),
929 c), and d) are subtidal salinity variations at S2, S3, and S4 stations.